SANDIA REPORT

Standoff Ultraviolet Raman Scattering Detection of Trace Levels of Explosives

Thomas A. Reichardt, Scott E. Bisson, and Thomas J. Kulp

Approved for public release; further dissemination unlimited.

⊞ Sandia National Laboratories

Standoff Ultraviolet Raman Scattering of Trace Levels of Explosives

Thomas A. Reichardt, Scott E. Bisson, and Thomas J. Kulp
Remote Sensing and Energetic Materials
Sandia National Laboratories
PO Box 969, MS 9056
Livermore, California 94551-0956

Abstract

Ultraviolet (UV) Raman scattering with a 244-nm laser is evaluated for standoff detection of explosive compounds. The measured Raman scattering albedo is incorporated into a performance model that focused on standoff detection of trace levels of explosives. This model shows that detection at ~100 m would likely require tens of seconds, discouraging application at such ranges, and prohibiting search-mode detection, while leaving open the possibility of short-range point-and-stare detection. UV Raman spectra are also acquired for a number of anticipated background surfaces: tile, concrete, aluminum, cloth, and two different car paints (black and silver). While these spectra contained features in the same spectral range as those for TNT, we do not observe any spectra similar to that of TNT.

CONTENTS

Figures

Tables

1. Introduction

Standoff detection of trace levels of explosive compounds has been held at the highest priority by defense and security concerns for the past decade [1,2]. As a result, investments have been made toward developing optical standoff detection approaches [3], including visible Raman scattering [4,5], laser-induced breakdown spectroscopy (LIBS) [6,7], photofragment (PF)-based approaches [8], coherent anti-Stokes Raman scattering (CARS) [9], and both passive and active infrared detection [10]. Thus far not one of these approaches has demonstrated the potential to achieve standoff detection of explosives traces with a field-deployable system on a variety of surfaces in realistic conditions. However, very recently the Swedish Defense Research Agency reported the use of ultraviolet (UV) Raman scattering for field-detection of vapor-phase nitromethane at 13 m [11]. Compared to the aforementioned alternatives, we note four differentiating features of UV Raman scattering: (1) Raman scattering is non-destructive, allowing repeatable optical sampling and signal averaging; (2) Raman scattering provides a unique chemical fingerprint of the molecule for improved specificity; (3) Raman scattering is a linear process, so the laser beam does not have to be focused at the sample to enhance the signal; (4) UV Raman scattering potentially allows the use of eye-safe laser fluences at UV wavelengths; (5) the use of UV lasers corresponds to Raman shifts of ~10 nm, less than the Stokes fluorescence shift from common materials, providing "fluorescence-free" measurements. While the first three advantages apply to Raman scattering in the visible wavelength range as well, the last two advantages are specific to UV probing. Also, compared to visible Raman scattering, UV Raman scattering from explosive compounds is expected to generate signals greater by several orders of magnitude due to the resonance enhancement of the Raman cross section [11-15].

In this work we evaluate the potential of standoff detection of explosives at trace levels by UV Raman scattering on typical surfaces, for use as either a stand-alone approach or as a confirmatory channel. We acquire UV Raman scattering of trace levels of the explosive TNT using a spectrally calibrated system. The measured results are implemented into a performance model to allow assessment of instrument performance. In addition to characterizing the photons resulting from the explosive compounds, the other two quantities required for detection assessment are the relative number and distinguishability of the photons generated by common backgrounds and interferences (in comparison to those generated by the explosive compounds). In other words, the ultimate performance of a detection system depends not only on capturing a sufficient number of photons from the explosive, but also on whether those photons both sufficiently exceed and are sufficiently distinguishable from those resulting from backgrounds and interferences.

2. Experiment

A Raman LIDAR consists of a co-located transmitter and receiver, which are responsible for projecting excitation light onto the target and collecting Raman scattering from it.   A simple schematic diagram of a Raman LIDAR is shown in Fig. 1.   The transmitter is a laser that is used in conjunction with formatting and steering optics (not shown) so that its beam intersects the field-of-view of the receiver at the point to be measured on the target. The receiver collects the scatter from the target using a large optic, such as a telescope, imaging the radiating target area onto the entrance aperture of some type of spectral-dispersion device, such as the Czerny-Turner spectrograph illustrated in Fig. 1.   A rejection filter is placed in the path between the receiver optic and the spectrograph, which rejects the strong backscatter at the laser frequency (i.e., photons not frequency-shifted by Raman scattering). The spectrograph disperses the light across an array detector, which records it and converts it to digital data.
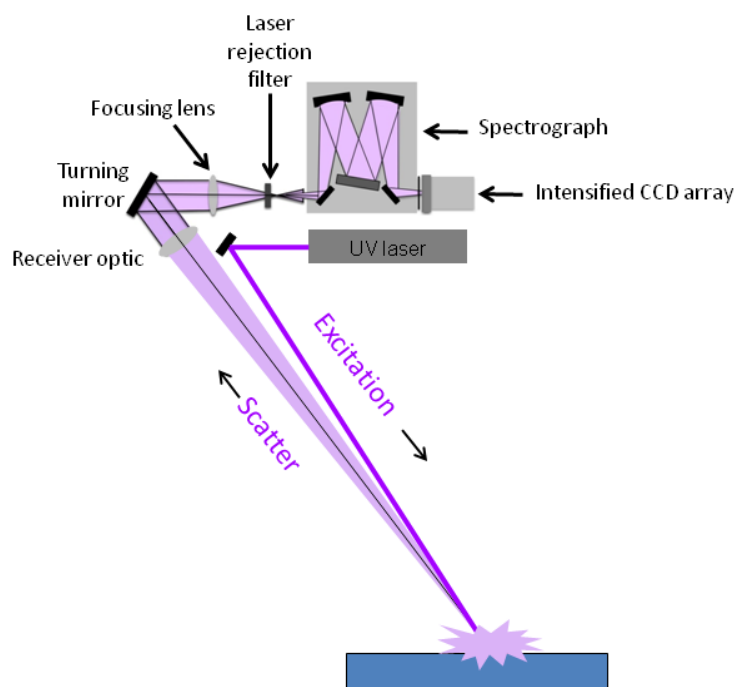
Fig. 1. Schematic diagram of Raman LIDAR instrument.

The radiometric properties of a LIDAR instrument are sufficiently well understood that one can accurately predicts its performance from appropriate laboratory measurements. This is the approach taken in this project. The following steps were taken to generate a confident performance estimate: (1) assembly of a lab-scale Raman transmitter and receiver; (2) calibration of the instrument in radiometric units; (3) comparison to published Raman cross-sections for selected explosives; and (4) extrapolation to field instrumentation and conditions. The results in each of these areas are described below.

2.1. Assembly of a lab-scale Raman transmitter and receiver

The laboratory Raman system developed for this project is shown in Fig. 2. The primary differences between it and a fieldable device lie in the type of transmitter and receiver optics used. Also, as shown in Fig. 2, the illumination and collection axes are orthogonal rather than nearly parallel, for reasons of mechanical convenience. Otherwise, the laser, spectrograph, and detector array all exhibit performance comparable to similar components that would be integrated into a fieldable device. The extrapolation of the performance of this system to that of a fieldable instrument (i.e., one which would use transmitter and receiver optics suitable for measuring a remote target) is straightforward.
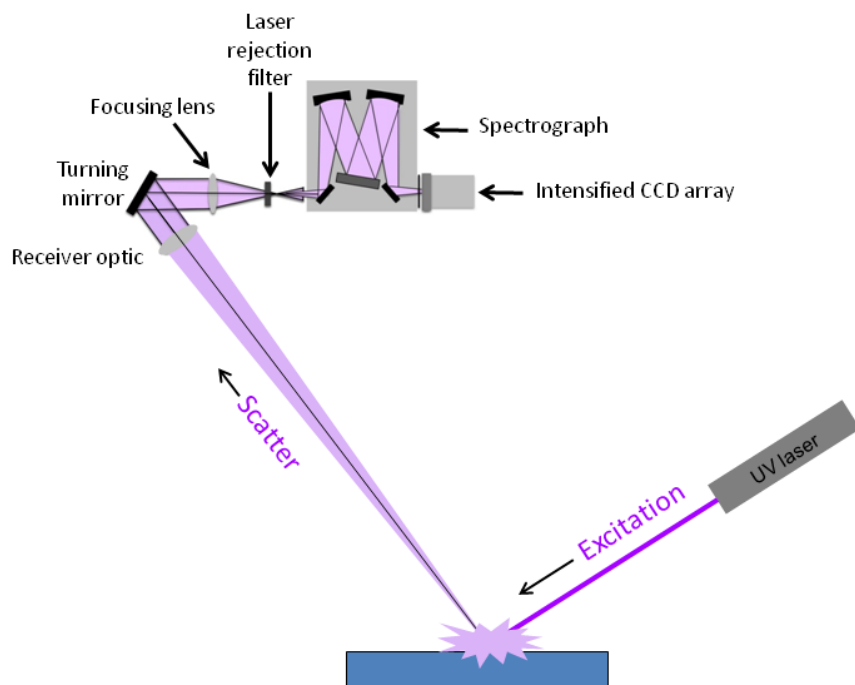
Fig. 2. Schematic diagram of laboratory Raman instrument.

The specific components of the lab system are described as follows. The probe laser is a frequency-doubled continuous-wave (cw) Ar-ion laser (Cambridge Lasers Laboratories Model 3500) producing 244-nm light. The laser is formatted to a diameter of about 1-mm at the sample. It is worth noting that earlier measurements were made with tighter focusing (about 0.2 mm diameter); however, that caused photodegradation of the explosive.

The receiver used for these measurements is only slightly modified from a system previously fabricated for the assessment of photofragment laser-induced fluorescence detection of surface-bound analytes [16,17]. The Raman scattering signal is collected by a pair of lenses (50-mm diameter; 300-mm focal length) that image the optical signal onto the entrance slit of a grating spectrograph. The spectrograph is a Czerny-Turner type (McPherson Inc., Chelmsford, MA; Model 218) that accepts light at f/5.3. Thus, its acceptance solid angle is slightly under-filled by that of the input light (f/6). Its entrance slit is oriented parallel to the laser beam axis and is adjusted to a width (typically 50 μm) to maintain acceptable spectral resolution. Once dispersed, the optical signal is imaged by the spectrograph onto the photocathode of an intensified charge-coupled device (ICCD) array detector (Andor Model DH501i-25F-04) having 1024×128 pixels. Spectroscopic measurements are conducted by on-chip binning of the array pixels in the vertical dimension to create a linear, 1024-element-long spectrum. The photocathode has a near-uniform quantum efficiency of about 13-15% over the

wavelength range of 200-300 nm (encompassing all signals measured in this project). The intensifier is gated to amplify photoelectron signals at gains of up to 400X for a 90-ms gate width.

2.2. Laboratory system calibration

The calibration of the relevant laser parameter (power) is accomplished using an ordinary laser power meter and requires no more discussion. The receiver calibration is carried out by placing a diffusely scattering material (Spectralon) at the sample location and illuminating it with a UV lamp of known radiance. This allows the measured counts on a channel of the ICCD to be related to radiance from the sample (W/sr) within the appropriate wavelength range intercepted by that channel.
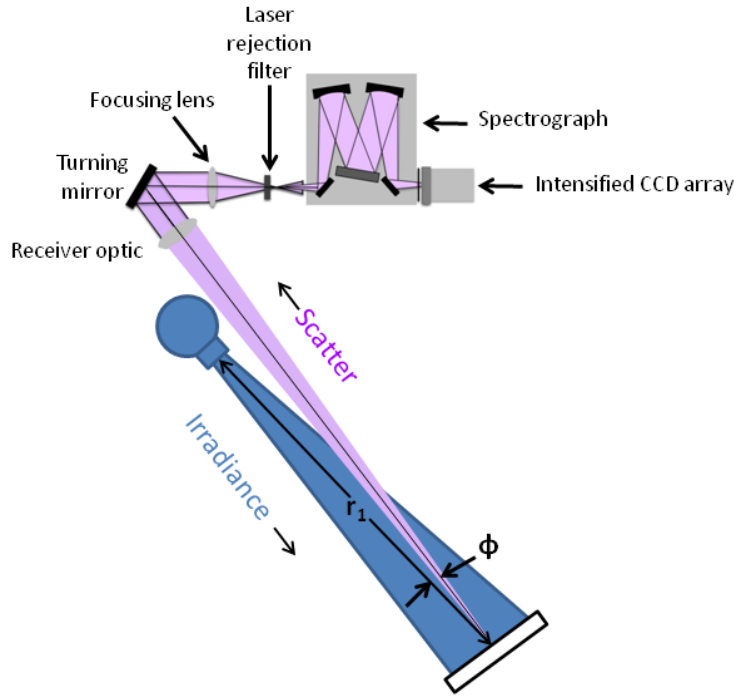
Fig. 3. Schematic diagram of the instrument configuration for spectral calibration.

The calibration function can be derived as follows. The manufacturer-supplied lamp spectral irradiance, $[I(\lambda)]_{\mathrm{mfg}}$ (Wcm^{-2}nm^{-1}), has been measured using a detector placed at 300 mm (r_{mfg}) distance from the lamp and oriented at normal incidence to its illumination axis. In the configuration illustrated in Fig. 3, the irradiance I' on the Spectralon target is

$$I'(\lambda, r_1, \phi) = [I(\lambda)]_{\mathrm{mfg}} \left(\frac{r_{\mathrm{mfg}}}{r_1}\right)^2 \cos(\phi), \qquad (1)$$

where the Spectralon target is oriented normal to the spectrometer axis and r_1 and ϕ are the distance (m) from the lamp to the Spectralon target and the angle of the incidence (rad) of the lamp illumination onto the Spectralon target, respectively.

The radiance, R (Wcm^{-2}nm^{-1}sr^{-1}) from the Spectralon to the spectrometer is

11

$$R(\lambda, r_1, \phi) = \frac{I'(\lambda, r_1, \phi) \cdot \rho(\lambda)}{\pi}, \tag{2}$$

where $\rho(\lambda)$ is the reflectance of the Spectralon, assumed to be a Lambertian reflector.

The ICCD photocathode area that corresponds to a single point in the calibration spectrum is

$$A_{pc} = w_{px}^2 \cdot n_h n_v, \tag{3}$$

where w_{px} is the width of a (square) pixel at the photocathode and n_v and n_h are the number of pixels binned in the vertical and horizontal dimensions. Because the spectrometer magnification is 1:1 between the slit plane and the photocathode plane, this is the same area that collects light at the slit plane. Also, because the Spectralon is imaged onto the slit plane at 1:1 magnification (identical lens focal lengths) at normal incidence, A_{pc} is equal to the area from which light is collected on the Spectralon.

The range of wavelengths spanned by this area is

$$\Delta\lambda = D \cdot n_h, \tag{4}$$

where D is the dispersion of the spectrometer (nm/pixel).

The calibration factor C (counts/J) that relates energy E (J) radiated by the sample (during a fixed observation time) to counts N measured by the detector channel is

$$N(\lambda)_\| = C(\lambda)_\| E(\lambda)_\|, \tag{5}$$

$$N(\lambda)_\perp = C(\lambda)_\perp E(\lambda)_\perp, \tag{6}$$

where Eq. (5) represents the calibration for parallel polarized light and Eq. (6) represents that for perpendicular polarization.

Because the measurements were all made with a depolarizer in the receiver light path, polarization can be ignored, and the calibration factor is

$$C(\lambda) = N(\lambda) / E(\lambda), \tag{7}$$

The energy radiated by the Spectralon that is available for the ith pixel to measure depends on the spectrum radiated, the spatial extent of the light on the Spectralon, and on the ratio of the slit with to the effective pixel size of the array (assuming all magnification is 1:1). The most rigorous way to quantify this available energy would be to generate an instrument spectral response function. For simplicity, we used a geometric approximation in which we assume that if N pixel fields of view are spanned by the slit (and the spectrum is flat over the corresponding wavelength range), then the irradiance on pixel i will be N times that within one pixel field-of-view.

The energy incident on pixel i during the time period τ (s) is

$$E_i = \left(\frac{w_{\text{slit}}}{w_{\text{px}}} \right) \cdot R(\lambda_i) \cdot A_{\text{pc}} \cdot \Delta\lambda \cdot \tau , \tag{8}$$

where w_{slit} is the width (μm) of the slit and λ_i is the wavelength (nm) corresponding to pixel i.

Rearranging previous equations gives

$$C(\lambda_i) = \frac{N(\lambda_i) \cdot \pi}{I(\lambda_i)_{\text{mfg}} \cdot \left(\dfrac{r_{\text{mfg}}}{r_1} \right)^2 \cdot \cos(\phi) \cdot \rho(\lambda_i) \cdot w_{\text{slit}} \cdot w_{\text{px}} \cdot n_h^2 \cdot n_v \cdot D \cdot \tau} . \tag{9}$$

The appropriate values for the instrument variables are listed in Table 1, and ρ is assumed to be spectrally flat and equal to 0.9. Inserting these values yields

$$C(\lambda) = \frac{N(\lambda) \cdot 5.42}{I(\lambda)_{\text{mfg}} \cdot w_{\text{slit}} \cdot D \cdot \tau} , \tag{10}$$

where the dependences of I, N, and C on λ are shown in Fig. 4. This equation allows the calibration function to be generated from a measurement of N at a given gain setting.

Table 1. Instrument variables for quantitative spectral calibraton.

INSTRUMENT VARIABLE	VALUE
r_{mfg}	300 mm
r_1	225 mm
ϕ	11.8°
w_{px}	26 x 10^{-4} cm
n_h	1
n_v	128
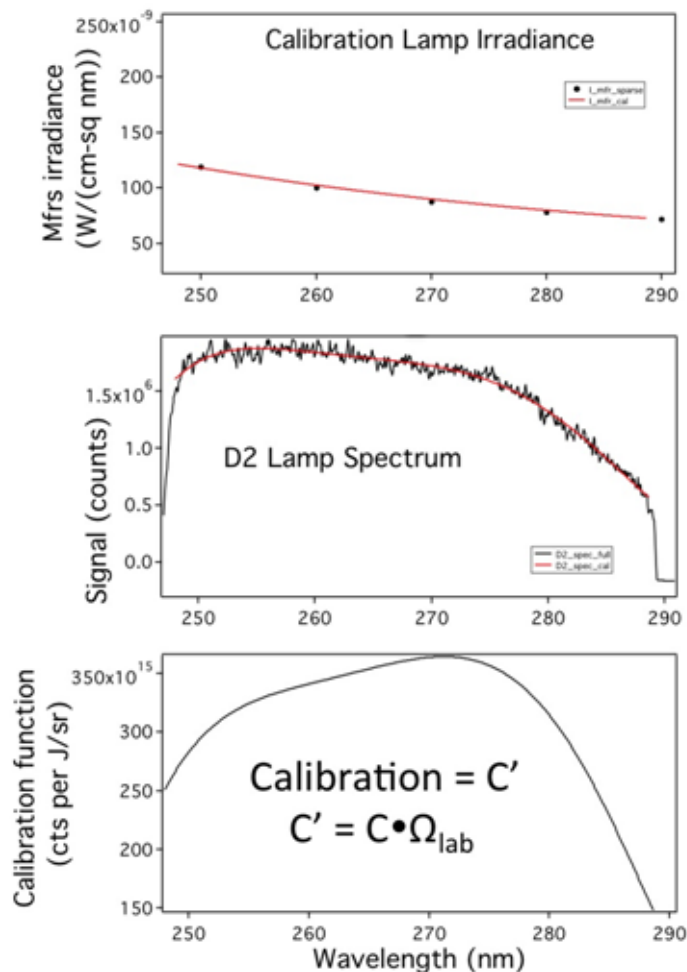
Fig. 4. Spectra for calibration procedure. The lamp source (top graph) provides a calibrated irradiance at a defined stand-off distance. This irradiance reflects from the calibrated reflectance surface to generate a radiance that is seen by the detector in units of counts. The counts per pixel (middle graph) can then be related to the energy reflected by the surface, providing the conversion between counts and J/sr (bottom graph).

2.3. Sample preparation

A droplet generator from Microfab Technologies (Plano, TX) is used to create samples with a uniform surface coverage. The Microfab system uses a piezoelectric-driven inkjet printing head to produce individual droplets (see Fig. 5) of highly repeatable size at a wide range of repetition rates. During deposition, the print head is mounted above a pair of orthogonal motor-driven stages (see Fig. 6) programmed to move the sample surface underneath the droplet deposition area in a raster pattern. The dimensions of the raster and the droplet release frequency are adjusted to create the desired coverage of simulant on the sample.

Fig. 5. Photograph of a droplet falling to the surface after generation by the inkjet.

Fig. 6. Photograph of the inkjet apparatus used to coat substrates.

.

3. Results

The goals of this work are to acquire quantitative UV Raman scattering spectra for comparison to literature results as well as to extend the performance of this approach to other detection scenarios. The former goal is accomplished through probing quantitative deposits of TNT with the calibrated Raman system, while the latter goal is accomplished through application of the LIDAR equation.
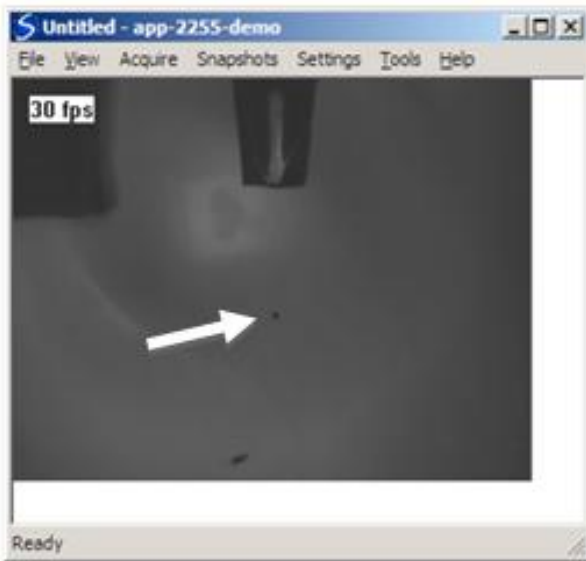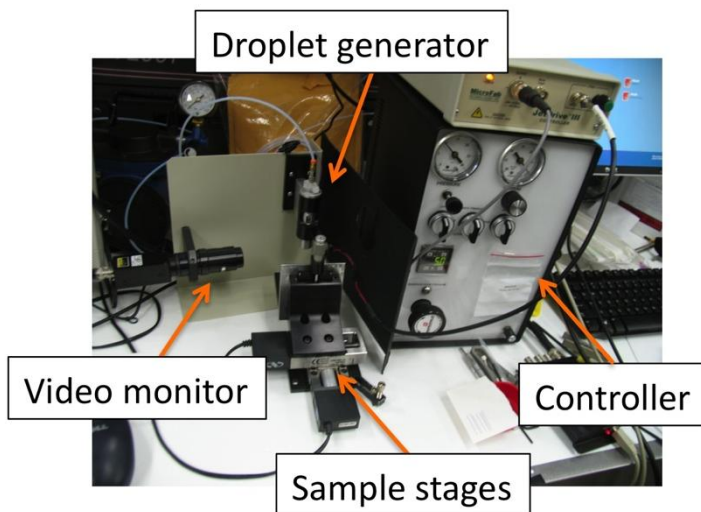
3.1. Raman scattering albedo

Calculation of the Raman scattering albedo directly follows from the calibration described in Section 2.2. We deposit concentrations of 1, 5, and 20 $\mu g/cm^2$ on a gold-coated disk. The disk is nominally rotated during data acquisition, but the signal is also assessed with a stationary target to evaluate any decrease in the signal due to photodegradation from repeated probing.

Figure 7 displays our calibrated Raman scattering spectrum of TNT on the gold substrate. Included is the spectrum of TNT presented by Short and Carter [18]. The spectral resolution of our detection system is lower than that of Short and Carter [18], and we therefore see some blending of the spectral features. Nevertheless, the main spectral features are evident in our acquired spectrum. The Raman signal is provided in terms of the Raman scattering albedo, which is spectrally integrated on a per-pixel basis.
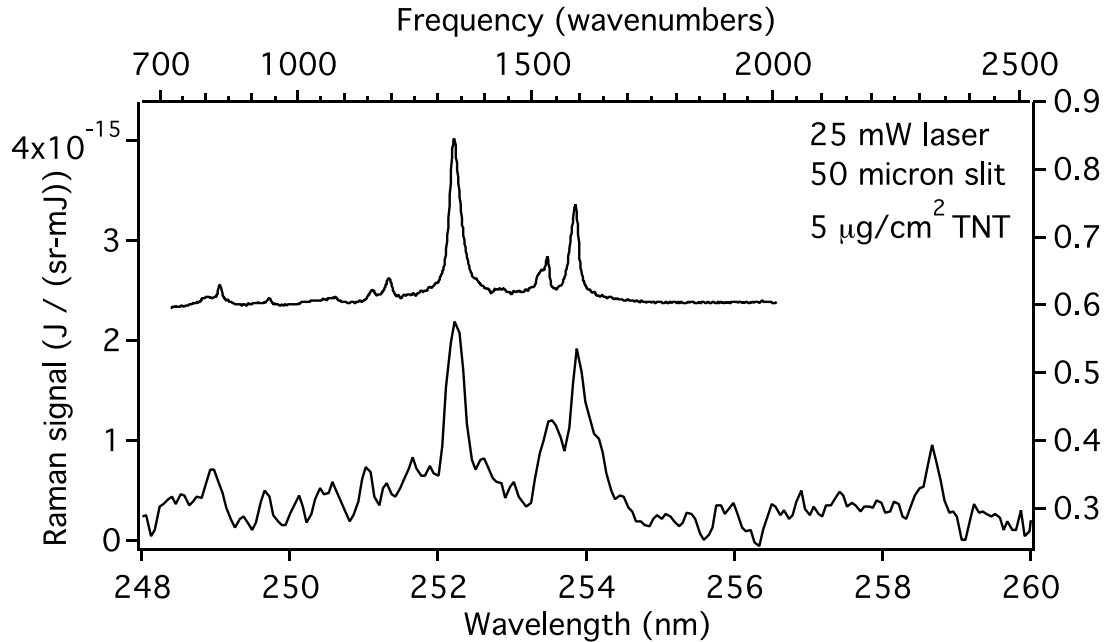

Fig. 7. Raman scattering signal (lower waveform) from TNT. Data from Short and Carter [18] (upper waveform) are shown for comparison.

We acquired data as presented in Fig. 7 for multiple deposits and for each one calculated the spectrally integrated Raman scattering albedo for the 1340-cm^{-1} feature. Our results are listed in Table 2.

Table 2. Raman scattering albedo measurements.

CONCENTRATION (μg/cm^2)	RAMAN SCATTERING ALBEDO (J/sr-mJ)	SUBSTRATE MOTION
1	1.5×10^{-14}	Rotating
5	1.8×10^{-14}	Rotating
5	1.3×10^{-14}	Rotating
5	1.1×10^{-14}	Rotating
20	1.9×10^{-14}	Rotating
20	1.6×10^{-14}	Stationary
20	1.6×10^{-14}	Stationary
20	6.7×10^{-15}	Stationary

3.2. Comparison with literature results

Several publications make reference to the resonance enhancement of Raman cross sections of explosive compounds. For comparison to our results, we have identified three publications reporting absolute cross sections for TNT in the wavelength region of our work. These are listed in Table 3. One [14] of these three studies detected UV Raman scattering of a TNT surface deposit, while the other two examined TNT diluted in a liquid solvent [12] and in the vapor phase [11]. Comparing these latter two results to the former, and to our data as well, requires considering the optical depth of the surface deposit. The absorption cross section of TNT is 6×10^{-17} cm^2/molecule at 244 nm [12], so with a molecular weight of 227.13 g/mol, the TNT concentration corresponding to the 1/e penetration length into the deposit ($C_{1/e}$) is

$$C_{1/e} = \frac{227.13 \text{g/mol}}{6.02 \times 10^{23} \text{ molecules/mol} \cdot 6 \times 10^{-17} \text{cm}^2/\text{molecule}} = 6 \times 10^{-6} \text{g/cm}^2 = 6 \,\mu\text{g/cm}^2 . \quad (11)$$

Note that the density of TNT is 1.654 g/cm^2, so the layer thickness $L_{1/e}$ corresponding to a 6μg/cm^2 deposit is only

$$L_{1/e} = \frac{6 \times 10^{-6} \text{g/cm}^2}{1.654 \text{g/cm}^3} = 4 \times 10^{-6} \text{cm} = 40 \,\text{nm}. \quad (12)$$

The probe beam is therefore attenuated to 1/e of the incident value after passing through the initial 40 nm of the deposit. Recognizing that the exiting signal will be similarly attenuated as well, this likely explains why the Raman scattering albedo is not a strong function of the deposited concentration for the range of concentrations assessed in our experiments we considered: for concentrations >6 μg/cm^2, signal will be collected from only the top layer of the deposit. Perhaps this also explains why the Raman scattering cross section of Nagli et al. [14] (measured on a surface deposit) is so much lower than the other two reported values. In the final row of Table 3, we include the Raman scattering cross section calculated from the 1 μg/cm^2 deposit.

Table 3. Raman scattering cross sections of TNT.

Study	Raman scattering cross section $(cm^2/sr\text{-}molecule) \times 10^{28}$	Sample probed
Nagli et al. [14]	1-2	Solid deposit
Sedlacek et al. [12]*	500	Sample diluted in solution
Ehlerding et al. [11]*	300	Vapor phase
This study	60	Solid deposit (1 μg/cm^2)

*Measured at 248 nm

3.3. Performance calculations

With quantitative knowledge of the Raman scattering albedo, a LIDAR model can be used to extrapolate our detection of explosives to other distances. The LIDAR equation calculating the number of signal photons S_{ph} is

$$S_{ph} = P_{laser} \cdot \Delta t \cdot \tau_{atm}(\lambda_{laser}) \cdot \tau_{atm}(\lambda_{signal}) \cdot a_{eff} \cdot \Omega_{field} \cdot S \cdot C \cdot Q / E_{photon}, \qquad (13)$$

where P_{laser} is the transmitted laser power (W), Δt is the integration time (s), $\tau_{atm}(\lambda_{laser})$ is the atmospheric transmission at the laser wavelength, $\tau_{atm}(\lambda_{signal})$ is the atmospheric transmission at the signal wavelength, a_{eff} is the effective Raman albedo (J/mJ-sr), S is the fraction of light that passes through the spectrograph slit, C is the detection efficiency (counts/J-sr), Q is the photons per count (as provided by the ICCD manufacturer), and E_{photon} is the photon energy at the signal wavelength (J). Assuming the laser is optimally matched to the slit ($S = 1$), with $C = C'/\Omega_{lab}$, and approximating equal atmospheric transmission τ_{atm} at the laser and signal wavelengths, we can re-write Eq. (13) as

$$S_{ph} = P_{laser} \cdot \Delta t \cdot \tau_{atm}^{2} \cdot a_{eff} \cdot \frac{\Omega_{field}}{\Omega_{lab}} \cdot C' \cdot Q / E_{photon}. \qquad (14)$$

Equation (14) can be used to extrapolate performance to other distances. The laser beam is assumed to be formatted into a sheet that matches the collection volume defined by the spectrograph slit (see Fig. 8). Rather than constraining performance by assuming a particular transmitted laser power, we instead constrain performance by limiting the laser intensity on the target to that used in the laboratory (see Fig. 9). This should avoid significant photodegradation of the sample during a point-and-stare measurement. Based on our prior LIDAR work, we assume that 300 photons must be collected to provide reliable detection. As illustrated by Fig. 10, the collection of this number of photons requires >10 s for all ranges considered.
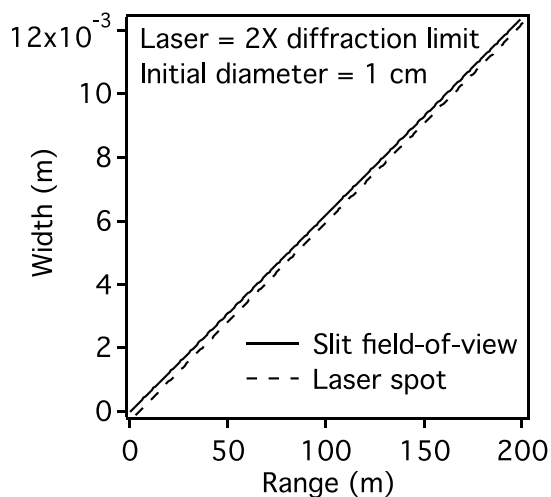
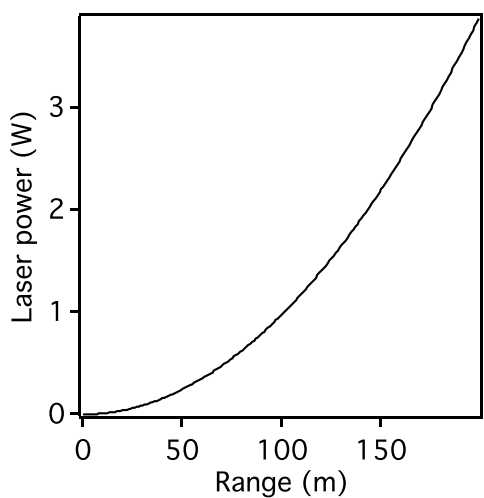Fig. 8. Laser spatial formatting for LIDAR calculations.

Fig. 9. Transmitted laser power for LIDAR performance calculations.

Fig. 10. Integration time required for detection.

Finally, the Raman scattering detection of explosives depends on both the signal strength as well as the distinguishability of the explosive signature from that of other materials. In an effort to assess the

distinguishability of the TNT Raman spectrum from common backgrounds, UV Raman spectra are also acquired for a number of anticipated background surfaces: tile, concrete, aluminum, cloth, and two different car paints (black and silver). While these spectra contained features in the same spectral range as those for TNT, we do not observe any spectra similar to that of TNT.
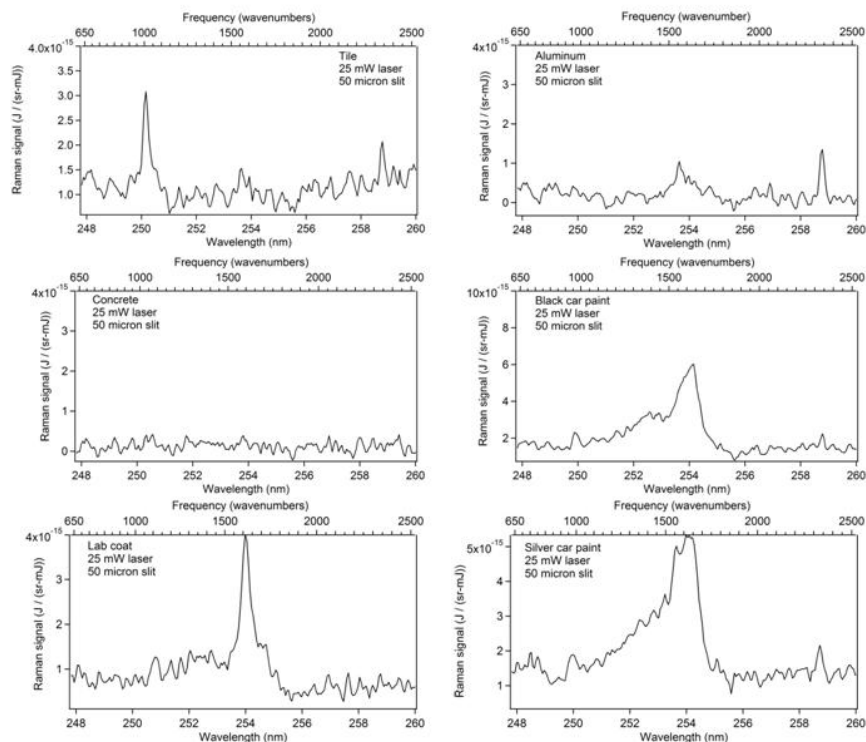
Fig. 11. Spectra of common backgrounds. While these spectra contained features in the same spectral range as those for TNT, they are not similar to that of TNT.

4. Summary

A calibrated continuous-wave (cw) ultraviolet (244-nm probe) Raman instrument was assembled and characterized. Quantitative amounts of TNT were deposited on a gold-coated surface and probed with the instrument. The signal level does not scale linearly with concentration. Rather, due to the absorption by TNT, with a 244-nm absorption cross section of 6×10^{-17} cm^2, the laser penetrates only ~40 nm into the sample. This corresponds to a deposit of 6 µg/cm^2, so deposits of this and higher concentrations are subject to optical thickness effects. For such deposits, rather than a Raman scattering cross section with units of cm^2/sr, it is better to consider a Raman scattering albedo, with units of J/sr-mJ. For the Raman scattering feature at 1340 cm^{-1}, we calculate a Raman scattering albedo of 1.5×10^{-14} J/sr-mJ.

Our measured Raman scattering albedo was incorporated into a performance model that focused on standoff detection of trace levels of explosives. This model showed that detection at ~100 m would likely require tens of seconds, discouraging application at such ranges, and prohibiting search-mode detection, while leaving open the possibility of short-range point-and-stare detection.
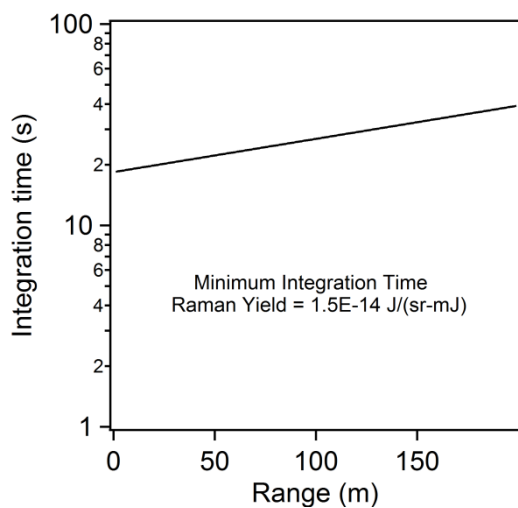
Finally, the Raman scattering detection of explosives depends on both the signal strength as well as the distinguishability of the explosive signature from that of other materials. In an effort to assess the distinguishability of the TNT Raman spectrum from common backgrounds, UV Raman spectra were also acquired for a number of anticipated background surfaces: tile, concrete, aluminum, cloth, and two different car paints (black and silver). While these spectra contained features in the same spectral range as those for TNT, we did not observe any spectra similar to that of TNT.

Future work is anticipated to focus on advancing the technology for application to realistic detection scenarios. Recognizing the advantages of implementing Raman scattering at UV wavelengths, the research community is making progress on UV laser sources [19] and spectrometers [20] optimized for Raman scattering. Yellampalle et al. [21,22] have reported the wavelength dependence of UV Raman-scattering albedos for a wide range of explosive compounds. Also, Raman scattering has already been implemented to image explosive-contaminated surfaces in both microscope imaging [23] and stand-off imaging [24,25] geometries.

References

1. A. A. Faust, C. J. de Ruiter, A. Ehlerding, J. E. McFee, E. Svinsas, and A. D. van Rheenen, "Observations on military exploitation of explosives detection technologies," Proc. of SPIE **8017**, 801716 (2011)

2. S. Désilets, N. Hô, P. Mathieu, J. R. Simard, E. Puckrin, J. M. Thériault, H Lavoie, F. Théberge, F. Babin, D. Gay, R. Forest, J. Maheux, G. Roy, and M. Châteauneuf, "Standoff detection of explosives, a challenging approach for optical technologies," Proc. of SPIE **8031**, 80312C (2011).

3. S. Wallin, A. Pettersson, H. Östmark, and A. Hobro, "Laser-based standoff detection of explosives: a critical review," Anal. Bioanal. Chem. **395**, 259-274 (2009).

4. M. L. Ramírez-Cedeño, W. Ortiz-Rivera, L. C. Pacheco-Londoño, and S. P. Hernández-Rivera, "Remote detection of hazardous liquids concealed in glass and plastic containers," IEEE Sensors Journal **10**, 693-698 (2010).

5. B. Zachhuber, G. Ramer, A. Hobro, E. t. H. Chrysostom, and B. Lendl, "Stand-off Raman spectroscopy: a powerful technique for qualitative and quantitative analysis of inorganic and organic compounds including explosives," Anal. Bionanal. Chem. **400**, 2439-2447 (2011).

6. J. L. Gottfried, F. C. De Lucia Jr., C. A. Munson, and A. W. Miziolek, "Laser-induced breakdown spectroscopy for detection of explosives residues: A review of recent advances, challenges, and future prospects," Anal. Bioanal. Chem. **395**, 283-300 (2009).

7. F. J. Fortes and J. J. Laserna, "The development of fieldable laser-induced breakdown spectrometer: No limits on the horizon," Spectrochimica Acta B **65**, 975-990 (2010)

8. C. M. Wynn, S. Palmacci, R. R. Kunz, and M. Aernecke, "Noncontact optical detection of explosive particles via photodissociation followed by laser-induced fluorescence," Opt. Express **19**, 18671-18677 (2011)

9. M. T. Bremer, P. J. Wrzesinski, N. Butcher, V. V. Lozovoy, and M. Dantus, "Highly selective standoff detection and imaging of trace chemicals in a complex background using single-beam coherent anti-Stokes Raman scattering," Appl. Phys. Lett. **99**, 101109 (2011).

10. A. Mukherjee, S. V. der Porten, and C. Kumar, N. Patel, "Standoff detection of explosive substances at distances of up to 150 m," Appl. Opt. **49**, 2072-2078 (2010).

11. A. Ehlerding, I. Johansson, S. Wallin, and H. Östmark, "Stand-off detection of vapor-phase explosives by resonance enhanced Raman spectroscopy," Proc. of SPIE **7835**, 783507 (2010).

12. A. J. Sedlacek, III, S. Chritesen, T. Chyba, and P. Ponsardin, "Application of UV-Raman spectroscopy to the detection of chemical and biological threats," Proc. of SPIE **5269**, 23-33 (2004).

13. G. Comanescu, C. K. Manka, J. Grun, S. Nikitin, and D. Zabetakis, "Identification of explosives with two-dimensional ultraviolet resonance Raman spectroscopy," Appl. Spectrosc. **62**, 833-839 (2008).

14. L. Nagli, M. Gaft, Y. Fleger, and M. Rosenbluh, "Absolute Raman cross-sections of some explosives: Trend to UV," Opt. Mater. **30**, 1747-1754 (2008).

15. P. Jander and R. Noll, "Automated detection of fingerprint traces of high explosives using ultraviolet Raman spectroscopy," Appl. Spectrosc. **63**, 559-563 (2009).

16. S. E. Bisson, J. M. Headrick, T. A. Reichardt, R. L. Farrow, T. J. Kulp, "A two-pulse, pump-probe method for short-range, remote standoff detection of chemical warfare agents," Proceedings of SPIE **8018**, 80180Q (2011).

17. T. J. Kulp, S. E. Bisson, T. A. Reichardt, J. M. Headrick, and R. L. Farrow, "Two-pulse rapid remote surface contamination measurement," Sandia Report SAND2010-7978 (2010).

18. B. J. Short and J. C. Carter, "Ultraviolet resonant Raman enhancements in the detection of explosives," Lawrence Livermore National Laboratory Report LLNL-TH-413751 (2009).

19. J. Kilmer, A. Iadevaia, and Y. Yin, "Laser sources for Raman spectroscopy," Proc. of SPIE **8039**, 803914 (2011).

20. N. Hagen and D. J. Brady, "Coded aperture DUV spectrometer for standoff Raman spectroscopy," Proc. of SPIE **7319**, 73190D (2009).

21. B. Yellampalle, M. Sluch, S. Asher, and B. Lemoff, "Explosive sensing using multiple-excitation-wavelength resonance-Raman scattering," Paper ATuE4 presented at the 2011 Conference on Lasers and Electro-Optics (CLEO 2011), Baltimore, MD, May 1-6, 2011.

22. B. Yellampalle, M. Sluch, S. Asher, and B. Lemoff, "Multiple-excitation-wavelength resonance-Raman explosives detection," Proc. of SPIE **8018**, 801819 (2011).

23. E. D. Emmons, A. Tripathi, J. A. Guicheteau, S. D. Christesen, and A. W. Fountain III, "Raman chemical imaging of explosive contaminated fingerprints," Appl. Spectrosc. **63**, 1197-1203 (2009).

24. M. Nordberg, M. Åkeson, H. Östmark, and T. E. Carlsson, "Stand-off detection of explosive particles by imaging Raman spectroscopy," Proc. of SPIE **8017**, 80171B (2011).

25. H. Östmark, M. Nordberg, and T. E. Carlsson, "Stand-off detection of explosives particles by multispectral imaging Raman spectroscopy," Appl. Opt. **50**, 5592-5599 (2011).

Distribution:

1	MS9056	Thomas A. Reichardt (electronic copy)
1	MS9056	Scott E. Bisson (electronic copy)
1	MS9056	Thomas J. Kulp (electronic copy)
1	MS9056	Wen L. Hsu (electronic copy)
1	MS9004	Duane Lindner (electronic copy)
1	MS0899	RIM – Reports Management, 9532 (electronic copy)